TECHNICAL PAPER

Wave propagation characteristics of the electrically GNP-reinforced nanocomposite cylindrical shell

Mostafa Habibi[1,2] · Masoud Mohammadgholiha[3] · Hamed Safarpour[4]

Abstract

In this article, wave propagation characteristics of a size-dependent graphene nanoplatelet (GNP) reinforced composite cylindrical nanoshell coupled with piezoelectric actuator (PIAC) and surrounded with viscoelastic foundation is presented. The effects of small scale are analyzed based on nonlocal strain gradient theory (NSGT) which is an accurate theory employing exact length scale parameter and nonlocal constant. The governing equations of the GNP composite cylindrical nanoshell coupled with PIAC have been evolved using Hamilton's principle and solved with assistance of the analytical method. For the first time in the current study, wave propagation electrical behavior of a GNP composite cylindrical nanoshell coupled with PIAC based on NSGT is examined. The results show that, by decreasing the PIAC thickness, extremum values of phase velocity occur in the lower values of the wave number. Another important result is that, by increasing GPL%, the effects of PIAC thickness on the phase velocity decrease. Finally, influence of PIAC thickness, wave number, applied voltage, and different GPL distribution patterns on phase velocity is investigated using mentioned continuum mechanics theory. Useful suggestion of this research is that for designing of a nanostructure coupled with PIAC attention should be given to PIAC thickness and applied voltage, simultaneously. The outputs of the current study can be used in the structural health monitoring and ultrasonic inspection techniques.

Keywords Wave propagation · Maxwell equation · Graphene nanoplatelet · Piezoelectric actuator · NSGT · Applied voltage

1 Introduction

Regarding the new progressions in science and technology, GNPs have engrossed significant attention. Some applications of GNP reinforcement are shown in Ref. [1]. Suna et al. [2] as an experimental study, compared the fracture behavior of functionally graded cemented carbide reinforced

Technical Editor: Wallace Moreira Bessa, D.Sc.

✉ Hamed Safarpour
  hamed_safarpor@yahoo.com

[1] Center of Excellence in Design, Robotics and Automation, School of Mechanical Engineering, Sharif University of Technology, Tehran, Iran

[2] Department of Mechanical Engineering, Sharif University of Technology, Tehran, Iran

[3] Civil Engineering Department, K.N. Toosi University of Technology, Tehran, Iran

[4] Department of Mechanics, Faculty of Engineering, Imam Khomeini International University, Qazvin, Iran

with and without the GNPs. In addition, they represented microstructure of the nanocomposites. Figure 1 shows the GNP layered in the matrix of the nanocomposites. They in this paper reported an attractive result that role of GNPs in the nanocomposites is the crack stopper (Fig. 2).

Nieto et al. [3] presented the effect of GNP value fraction on grain size and mechanical property of the GNP-reinforced tantalum composite. Their result showed the SEM micrographs of the tantalum/GNP composites (Fig. 3). The grain size of tantalum/GNP composites with different value fractions of GNP is shown in Fig. 4. It should be noted that the results of Fig. 4 are obtained from micrographs similar to Fig. 3.

According to Figs. 3 and 4, by increasing value fraction of GNP into nanocomposite, it is a reason for production finer grain. It is worth to mention that grain refinement has an important role on the mechanical properties. Rafiee et al. [4] compared the mechanical properties of epoxy nanocomposites refined with 1% value fraction of single-walled carbon nanotubes (SWNT), multiwalled carbon nanotube (DWNT) and GNP with each other. Their results show that
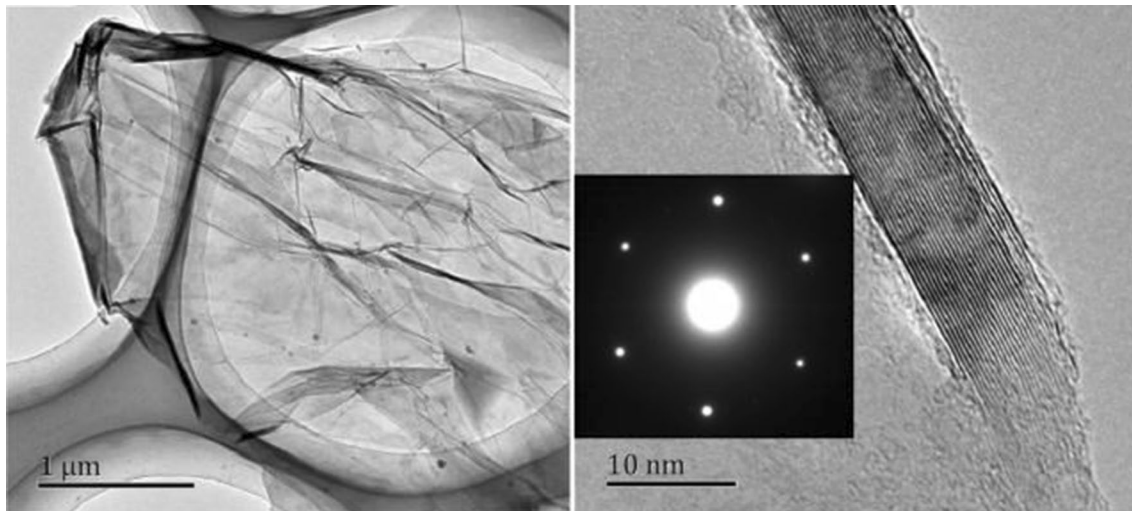
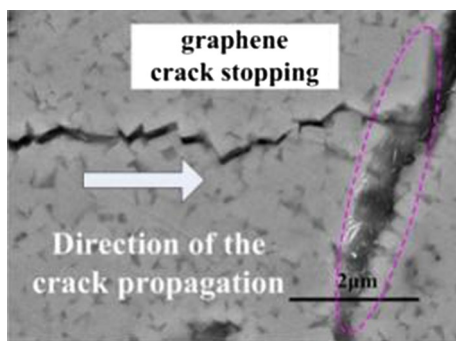**Fig. 1** The GNP layered in the matrix of the nanocomposites

Fig. 2 Role of GNPs as the crack stopper in the nanocomposites

Young's modulus, ultimate tensile strength, fracture toughness, fracture energy and fatigue resistance of the GNPs are more than other materials (Fig. 5). So that GNP materials can be replaced instead of SWNTs and MWNTs in many applications.

Researches proved that subjoining even a very meager amount of graphene into primary polymer matrix can desperately improve its mechanical, thermal and electrical properties [5–9]. It is worse to mention that nanostructures reinforced with GNP are more applicable in engineering design, so focus on dynamic modeling of the nanostructure with GNP reinforcement is useful and important. Furthermore, polymer matrix reinforced by various types of nanofillers is one of the most efficient and easily extruded nanocomposite materials with a wide range of applications such as field effect transistors, electromechanical actuators, biosensors and chemical sensors, solar cells, photoconductor and superconductor devices. For this reason, the investigation of their mechanical characteristics is a great interest for engineering design and manufacturing. In the field reinforcement

structures, Habibi et al. [10–14] with the aid of some methods improved the mechanical property of macro-structures. Dong et al. [15] presented an analytical study on linear and nonlinear vibration characteristics and dynamic responses of spinning FG graphene-reinforced thin cylindrical shells with various boundary conditions and subjected to a static axial load. Dong et al. [16] investigated the buckling behavior of FG graphene-reinforced porous nanocomposite cylindrical shells with spinning motion and subjected to a combined action of external axial compressive force and radial pressure. Dong et al. [17] concerned with free vibration characteristics of the functionally graded graphene-reinforced porous nanocomposite cylindrical shell with spinning motion. In their result section, detailed parametric studies on natural frequencies and critical spinning speeds of the GPL-reinforced porous nanocomposite cylindrical shell are carried out, especially, effect of initial hoop tension on vibration characteristics of the spinning cylindrical shell is numerically discussed. Jang et al. [18] presented the postbuckling and buckling behaviors of FG multilayer nanocomposite beams reinforced with graphene platelets (GNPs). They investigated that GNPs have a remarkable reinforcing effect on the buckling and postbuckling of nanocomposite beams. In another work, Feg et al. [19] found out nonlinear bending behavior of a novel class of multilayer polymer composite beams reinforced with graphene platelets (GNPs). They studied that beam with a higher value fraction of GNPs and symmetric distribution in such a way is less sensitive to the nonlinear deformation.

None of the above researches have taken size effects into account in wave propagation analysis of structures. Continuum mechanics theories including classical theory [20, 21] and size-dependent theories are used to model micro/ nanostructures. As classical theory does not consider
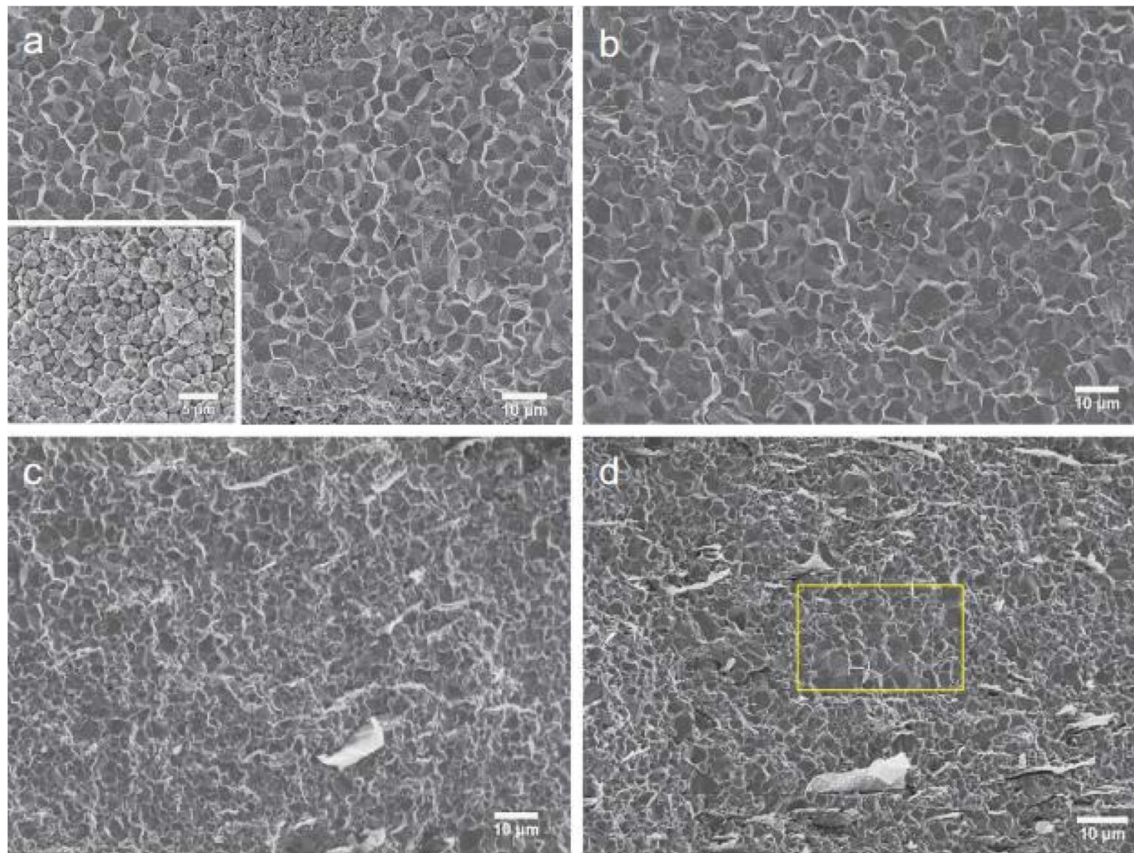
Fig.. 3 SEM micrographs of the pure tantalum and tantalum/GNP composites. **a** Pure tantalum, **b** 1 wt% GNP, **c** 3 wt% GNP, **d** 5 wt% GNP [3]
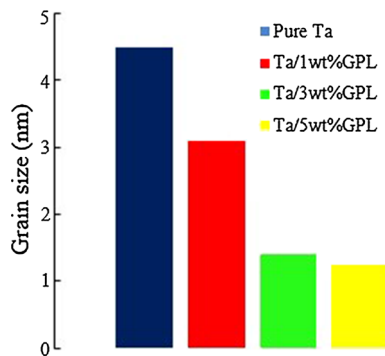

Fig. 4 The grain size of tantalum/GNP composites with different value fraction of GNP [3]

Fig. 5 Ultimate tensile strength and Young modulus for the baseline epoxy and GNP/epoxy, MWNT/epoxy, and SWNT/epoxy nanocomposites [4]

submicron discontinuities of structure, so it cannot capture size-dependent effects when scale turns to micro or nano. Size-dependent theories including nonlocal [22–30], strain gradient [31, 32] and couple stress [33–38] theories are better choices and present more accurate outputs in these cases. It should be noted that mentioned theories consist of size-dependent parameters which their exact values must be determined by experiment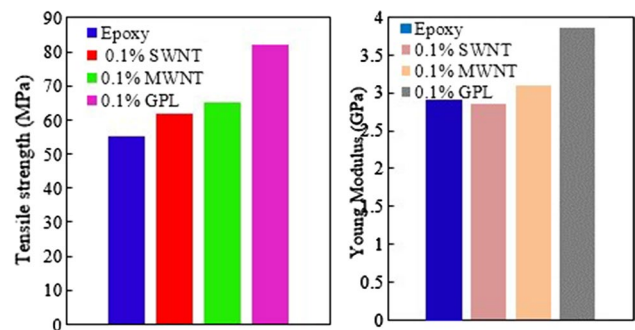al data or numerical simulations [39–41]. For simple structures such as graphene sheets or carbon nanotubes, production of material for experiment or simulation is a straightforward process, but for composite structures, the process becomes complicated and encourages the researchers to approximate the models through mathematics and theories. Gul and Aydogdu [42] employed some length scale-dependent theories for investigation of wave propagation in double-walled carbon nanotubes. As

a comparative research, they compared doublet mechanics results with classical elasticity, strain gradient theory, nonlocal theory and lattice dynamics. Experimental wave frequencies and doublet mechanics theory of graphite have good agreement with each other, so they showed that doublet mechanics theory has higher accuracy.

Ard and Aydogdu [43] studied torsional wave propagation for a multiwalled carbon nanotubes in the framework of Eringen's nonlocal elasticity theory. They considered effect of van der Waals interaction and reported that the interaction has an important role in torsional wave propagation. In another work, Islam et al. [44] represented size effects on torsional wave propagation of circular nanostructure, such as nanoshafts, nanorods and nanotubes. They demonstrated the significance of considering the integral nonlocal model and nanoscale relations in dispersion characteristics of circular nanostructures. Aydogdu [45] employed nonlocal elasticity theory for studying longitudinal wave propagation in multiwalled carbon with including van der Waals force effect in the axial direction. In the result of this paper, the effects of various parameters on wave propagation were examined in detail. In recent years, incorporating the local and nonlocal curvatures in constitutive relations, NSGT has emerged. Based on this theory, the stress of submicron-scale structures appears in both nonlocal stress and pure strain gradient stress fields. Lim et al. [46] used thermodynamic framework to derive NSGT equations, so that the higher-order nonlocal parameters and the nonlocal gradient length coefficients were considered.

Applications of NSGT in vibration analysis of nanostructures [47–49] have attracted many researcher's attentions. Zeighampour et al. [50] investigated wave propagation in double-walled carbon nanotube surrounded by Winkler foundation using the nonlocal strain gradient theory. In their results, nonlocal strain gradient theory and classical theory were compared in terms of the influences of nonlocal and material length scale parameters, wave number, fluid velocity and stiffness of elastic foundation on phase velocity. In another work [51], they modeled a composite cylindrical micro/nanoshells and studied the variation of phase velocity versus material length scale parameters and nonlocal constant. According to that paper, an increase in material length scale increases the phase velocity while nonlocal parameter acts vice versa. Zeighampour et al. [52] conducted a wave propagation study on a thin cylindrical nanoshell surrounded by visco-Pasternak foundation based on nonlocal strain gradient theory. The viscoelastic properties were modeled by Kelvin–Voigt theory. They indicated that the structure has a better stability condition using strain gradient theory in comparison with classical theory. In the field of the wave propagation behavior of a structure coupled with piezoelectric actuators, Lat. Am et al. [53] studied wave propagation of the two-layer piezoelectric composite structure. As

a parametric study, they in this work showed the effects of volume fraction, thickness and elastic constant on the wave dispersion of the structure. Arani et al. [54] investigated wave dispersion of the FG carbon nanotube-reinforced piezoelectric composite. They in this work included the visco-Pasternak in their mathematical modeling. The structure was subjected to magnetic and electric fields. Their results showed that external voltage has a significant effect on the wave desperation behavior. Zhou [55] modeled the piezoelectric cylindrical shells and investigated surface effect on wave dispersion of the nanostructure. Their results presented that at the higher mode surface effect has a significant effect on the wave propagation of the structure. Bishe et al. [56] presented wave propagation in smart laminated composite cylindrical shells reinforced with carbon nanotubes in hygrothermal environments. They investigated the effects of temperature/moisture variation, CNT volume fraction and orientation, piezoelectricity, shell geometry, stacking sequence and material properties of the host substrate laminated composite shell at different axial and circumferential wave numbers and the results of their work showed that the temperature/moisture variation influences moderately on the dispersion solutions of smart laminated CNT-reinforced composite shells. Bishe et al. [57] focused on the wave propagation in piezoelectric cylindrical composite shells reinforced with angled and randomly oriented CNTs. Bishe et al. [58] studied and analyzed wave propagation in a piezoelectric cylindrical composite shell reinforced with CNTs by using the Mori–Tanaka micromechanical model and considering the transverse shear effects and rotary inertia via the first-order shear deformation shell theory. Bishe et al. [59] investigated wave behavior in a piezoelectric coupled laminated fiber-reinforced composite cylindrical shell by considering the transverse shear effects and rotary inertia. In the results of their work presented a comparison of dispersion solutions from different shell theories with different axial and circumferential wave numbers and piezoelectric layer thickness is provided to illustrate the transverse shear and rotary inertia effects on wave behavior of a laminated fiber-reinforced composite shell. Guo et al. [60] analyzed the effects of FG interlayers on the wave propagation in covered piezoelectric/piezomagnetic cylinders. They in this work showed that high-order modes are more sensitive to the gradient interlayers, while the low-order modes are more sensitive to the electromagnetic surface conditions. The wave propagation of the porous FG plates with the aid of some shear deformation theories was analyzed by Yahia et al. [61]. As an application, they showed that their results are useful for ultrasonic inspection. Also, they presented the effect of porosity on the wave propagation behavior of the structure. The present study investigates the wave propagation piezoelectric behavior of a GPLRC cylindrical nanoshell coupled with PIAC based on NSGT with considering the

calibrated values of nonlocal constant and material length scale parameter for the first time. In this regard, influence of wave number, critical applied voltage and GNP distribution pattern on phase velocity are investigated using mentioned continuum mechanics theory.

2 Mathematical modeling

In Fig. 6, a GNPRC cylindrical nanoshell coupled with PIAC is modeled. The thickness, length and the middle surface radius of the cylindrical shell are $h_{\text{eff}}(h + h_{\text{p}})$, L and R, respectively. In addition, the nanostructure is subjected to the electric potential (V) and z-axis is the poling direction. The cylindrical nanoshell is made of a new composite material.

2.1 Nonlocal strain gradient theory

According to the nonlocal strain gradient theory, the general constitutive equation can be expressed as follows [62]:

$$(1 - \mu^2 \nabla^2) t_{ij} = C_{ijck} (1 - l^2 \nabla^2) \varepsilon_{ck} \tag{1}$$

where $\nabla^2 = \partial^2/\partial x^2 + \partial^2/\partial(\theta R)^2$, t_{ij}, ε_{ck} and C_{ijck} are the components of nonlocal strain gradient stress tensor, strain tensor and elasticity tensor, respectively. Nonlocal strain gradient stress tensor is explained in the following form:

$$t_{ij} = \sigma_{ij} - \nabla \sigma_{ij}^{(1)} \tag{2}$$

where σ_{ij} and $\sigma_{ij}^{(1)}$ are classical and size-dependent stresses, respectively. The μ and l parameters denote the influence of noninvariant stress field and higher-order strain gradient stress field. The calibrated values of mentioned

size-dependent parameters are determined through experimental studies. These parameters are considered to be constant and stable for the proposed model. The strain tensor is written as:

$$\varepsilon_{ij} = \frac{1}{2} \left(u_{i,j} + u_{j,i} \right) \tag{3}$$

2.2 Constitutive equations for nanocomposite core and piezoelectric layers

The matrix of nanostructure is composed of GNPRC materials. The volume fraction functions of these materials have been represented by

Pattern1: $\quad V_{\text{GPL}}(k) = V_{\text{GPL}}^* \tag{4}$

Pattern2: $\quad V_{\text{GPL}}(k) = 2V_{\text{GPL}}^* |2k - N_{\text{L}} - 1|/N_{\text{L}} \tag{5}$

Pattern3: $\quad V_{\text{GPL}}(k) = 2V_{\text{GPL}}^* \left[1 - \left(|2k - N_{\text{L}} - 1|/N_{\text{L}} \right) \right]$
$$\tag{6}$$

Pattern4: $\quad V_{\text{GPL}}(k) = 2V_{\text{GPL}}^* (2k - 1)/N_{\text{L}} \tag{7}$

where k is number of layers of the microstructure, N_{L} is the total number of layers and V_{GPL}^* is the total volume fraction of GNPs. The relation between V_{GPL}^* and their weight fraction g_{GPL} can be expressed by:

$$V_{\text{GPL}}^* = \frac{g_{\text{GPL}}}{g_{\text{GPL}} + (\rho_{\text{GPL}}/\rho_{\text{m}})(1 - g_{\text{GPL}})} \tag{8}$$

in which ρ_{GPL} and ρ_{m} are the mass densities of GNP and the polymer matrix. Based on Halpin–Tsai model, the elastic modulus of composites reinforced with randomly GNP approximated by [63]:

Fig. 6 Geometry of GNPRC cylindrical nanoshell coupled with PIAC
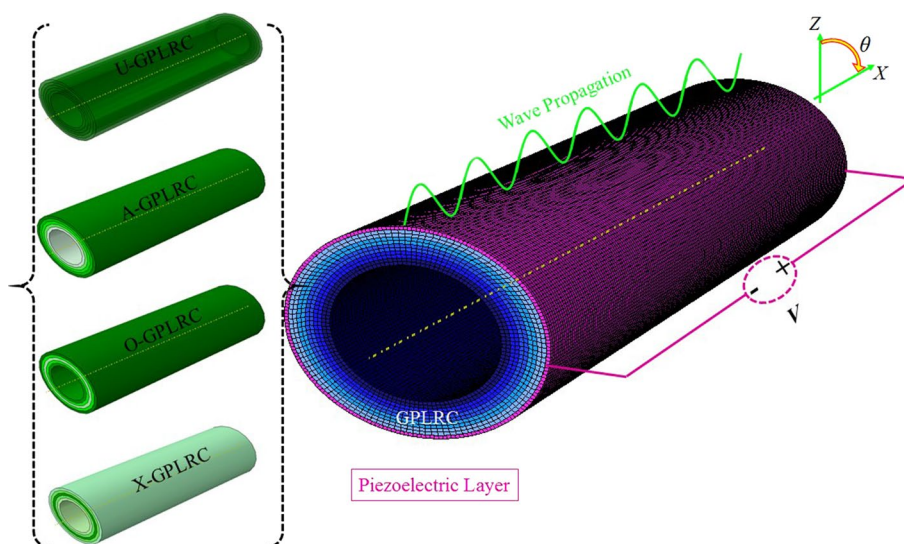
$$E = \frac{3}{8}E_L + \frac{5}{8}E_T,$$
$$E_L = \frac{1 + \xi_L n_L V_{GPL}}{1 - n_L V_{GPL}} E_m, \quad E_T = \frac{1 + \xi_T n_T V_{GPL}}{1 - n_T V_{GPL}} E_m \quad (9)$$

where E is effective modulus of composites reinforced with GNPs and E_L and E_T are the longitudinal and transverse moduli for a unidirectional lamina. In Eq. (9), the GNP geometry factors (ξ_L and ξ_T) and other parameters are given by:

$$\xi_L = 2(\mathbb{Z}_{GPL}/h_{GPL}), \quad \xi_T = 2(b_{GPL}/h_{GPL}),$$
$$n_L = \frac{(E_{GPL}/E_m) - 1}{(E_{GPL}/E_m) + \xi_L}, \quad n_T = \frac{(E_{GPL}/E_m) - 1}{(E_{GPL}/E_m) + \xi_T} \quad (10)$$

where $\mathbb{Z}_{GPL}, h_{GPL}, b_{GPL}$ are the average length, thickness and width of the GPLs. By using the rule of mixture, mass density ρ_c and Poisson's ratio v_c of the GPL/polymer nanocomposite are expressed as:

$$\bar{E} = E_{GPL}V_{GPL} + E_M V_M,$$
$$\bar{\rho} = \rho_{GPL}V_{GPL} + \rho_M V_M,$$
$$\bar{v} = v_{GPL}V_{GPL} + v_M V_M,$$
$$\bar{\alpha} = \alpha_{GPL}V_{GPL} + \alpha_M V_M. \quad (11)$$

The mechanical properties of the GPLR cylindrical shell can be obtained by [63]. In addition, the stress–strain relation of the composite core can be expressed as follows:

$$\begin{bmatrix} \sigma_{xx} \\ \sigma_{\theta\theta} \\ \sigma_{zz} \\ \sigma_{x\theta} \\ \sigma_{xz} \\ \sigma_{\theta z} \end{bmatrix} = \begin{bmatrix} \bar{Q}_{11} & \bar{Q}_{12} & \bar{Q}_{13} & 0 & 0 & 0 \\ \bar{Q}_{12} & \bar{Q}_{22} & \bar{Q}_{23} & 0 & 0 & 0 \\ \bar{Q}_{13} & \bar{Q}_{23} & \bar{Q}_{33} & 0 & 0 & 0 \\ 0 & 0 & 0 & \bar{Q}_{44} & 0 & 0 \\ 0 & 0 & 0 & 0 & \bar{Q}_{55} & 0 \\ 0 & 0 & 0 & 0 & 0 & \bar{Q}_{66} \end{bmatrix} \begin{bmatrix} \varepsilon_{xx} \\ \varepsilon_{\theta\theta} \\ \varepsilon_{zz} \\ \varepsilon_{x\theta} \\ \varepsilon_{xz} \\ \varepsilon_{\theta z} \end{bmatrix} \quad (12)$$

where the stiffness coefficients (Q_{ij}) are obtained in Ref. [64].

2.3 Piezoelectric layers

The relationships between the stress and strain for the piezoelectric layers are written as follows:

$$\begin{Bmatrix} \sigma_{xx} \\ \sigma_{\theta\theta} \\ \sigma_{x\theta} \\ \sigma_{\theta z} \\ \sigma_{xz} \end{Bmatrix} = \begin{bmatrix} c_{11} & c_{12} & 0 & 0 & 0 \\ c_{12} & c_{22} & 0 & 0 & 0 \\ 0 & 0 & c_{66} & 0 & 0 \\ 0 & 0 & 0 & c_{55} & 0 \\ 0 & 0 & 0 & 0 & c_{44} \end{bmatrix} \cdot \begin{Bmatrix} \varepsilon_{xx} \\ \varepsilon_{\theta\theta} \\ \varepsilon_{x\theta} \\ \varepsilon_{\theta z} \\ \varepsilon_{xz} \end{Bmatrix} - \begin{bmatrix} 0 & 0 & e_{31} \\ 0 & 0 & e_{32} \\ 0 & 0 & 0 \\ 0 & e_{24} & 0 \\ e_{25} & 0 & 0 \end{bmatrix} \begin{Bmatrix} E_x \\ E_\theta \\ E_z \end{Bmatrix} \quad (13)$$

$$\begin{Bmatrix} D_x \\ D_\theta \\ D_z \end{Bmatrix} = \begin{bmatrix} 0 & 0 & 0 & 0 & e_{15} \\ 0 & 0 & 0 & e_{24} & 0 \\ e_{31} & e_{32} & 0 & 0 & 0 \end{bmatrix} \cdot \begin{bmatrix} \varepsilon_{xx} \\ \varepsilon_{\theta\theta} \\ \varepsilon_{x\theta} \\ \varepsilon_{\theta z} \\ \varepsilon_{xz} \end{bmatrix} + \begin{bmatrix} s_{11} & 0 & 0 \\ 0 & s_{22} & 0 \\ 0 & 0 & s_{33} \end{bmatrix} \begin{Bmatrix} E_x \\ E_\theta \\ E_z \end{Bmatrix} \quad (14)$$

where $c_{ijkl}, e_{mij}, d_{in}, p_i, \beta_{ij}$ and s_{im} are the elasticity matrix, piezoelectric constants, pyroelectric constants, thermal moduli and dielectric constants, respectively. D_i and E_m are electric displacement and electric fields strength of the piezoelectric cylindrical shell, respectively. The electric and magnetic field strength, i.e., E_x, E_θ, E_z which are used in Eqs. (13) and (14) could be expressed as follows:

$$E_x = -\frac{\partial \tilde{\Phi}}{\partial x}$$
$$E_\theta = -\frac{1}{R + z}\frac{\partial \tilde{\Phi}}{\partial \theta} \quad (15)$$
$$E_z = -\frac{\partial \tilde{\Phi}}{\partial z}.$$

Ghadiri et al. [64] investigated that the potential of electric could be assumed as:

$$\tilde{\Phi}(x, \theta, z, t) = -\cos(\beta z)\phi(x, \theta, t) + \frac{2z\phi_0}{h} \quad (16)$$

in which $\beta = \pi/h$, $\tilde{\Psi}$ and $\tilde{\Phi}$ are the initial external electric and magnetic potential, respectively.

2.4 Displacement field of the cylindrical shell

Based on the first shear deformation theory, the displacement field of the cylindrical shell is as below:
$$U(x, \theta, z, t) = u(x, \theta, t) + z\psi_x(x, \theta, t)$$
$$V(x, \theta, z, t) = v(x, \theta, t) + z\psi_\theta(x, \theta, t) \quad (17)$$
$$W(x, \theta, z, t) = w(x, \theta, t)$$

Here, $U(x, \theta, z, t)$, $V(x, \theta, z, t)$ and $W(x, \theta, z, t)$ indicate displacements of the neutral surface along x, θ and z directions, respectively, and ψ_x, ψ_θ show rotations of a cross section around θ and x-direction. Substituting Eq. (17) into Eq. (3), the components of the strain tensor are extracted as follows:

$$\varepsilon_{xx} = \frac{\partial u}{\partial x} + z\frac{\partial \psi_x}{\partial x}$$
$$\varepsilon_{\theta\theta} = \frac{1}{R}\frac{\partial v}{\partial \theta} + \frac{z}{R}\frac{\partial \psi_\theta}{\partial \theta} + \frac{w}{R}$$
$$\varepsilon_{xz} = \frac{1}{2}\left(\psi_x + \frac{\partial w}{\partial x}\right) \quad (18)$$
$$\varepsilon_{x\theta} = \frac{1}{2}\left(\frac{1}{R}\frac{\partial u}{\partial \theta} + \frac{\partial v}{\partial x}\right) + \frac{z}{2}\left(\frac{1}{R}\frac{\partial \psi_x}{\partial \theta} + \frac{\partial \psi_\theta}{\partial x}\right)$$
$$\varepsilon_{\theta z} = \frac{1}{2}\left(\psi_\theta + \frac{1}{R}\frac{\partial w}{\partial \theta} - \frac{v}{R}\right)$$

2.5 Derivation of governing equations and boundary conditions

According to the FSDT and nonlocal strain gradient theory, the governing equations and corresponding boundary conditions of the cylindrical shell can be extracted using the Hamilton principle as follows:

$$\int_{t_1}^{t_2} (\delta T - \delta \Pi_s + \delta \Pi_w) \, dt = 0 \tag{19}$$

where K is the kinetic energy, Π_s is strain energy and Π_w is the work done corresponding to external applied forces which are, respectively, expressed as:

2.6 External work

The external work on the GNPRC cylindrical nanoshell with piezoelectric layers is due to external electrical load. So that the first variation of the work done corresponding to the external electric applied force:

$$\Pi_w = \iint_A \left[(N_1^P) w_{,x} \delta w_{,x} + (N_2^P) v_{,x} \delta v_{,x} \right] R \, dx \, d\theta \tag{20}$$

where N_i^p is external electric loads. The electric loads could be obtained as follows [64]:

$$N_1^P = N_2^P = -2 \left(e_{31} - \frac{c_{13} e_{33}}{c_{33}} \right) \phi_0 \tag{21}$$

2.7 Kinetic energy

$$T = \frac{1}{2} \int_Z \iint_A \rho \left\{ \dot{u}^2 + \dot{v}^2 + \dot{w}^2 \right\} R \, dz \, dx \, d\theta \tag{22}$$

2.8 Strain energy

According to nonlocal strain gradient theory, the strain energy is defined as follows [65]:

By substituting Eqs. (13), (14) and (18) into Eq. (23), the variation of strain energy can be explained as:

$$\tag{23}$$

$$\Pi_s = \frac{1}{2} \iiint_{V_{core}} \left(\sigma_{ij} \varepsilon_{ij} + \sigma_{ij}^{(1)} \nabla \varepsilon_{ij} \right) dV_{core}$$

$$+ \iiint_{V_{piezolayer}} (D_x \delta E_x + D_\theta \delta E_\theta + D_z \delta E_z) dV_{piezolayer}$$

$$\delta \Pi_s = \iint_A \left\{ \begin{array}{l} N_{xx} \frac{\partial}{\partial x} \delta u + M_{xx} \frac{\partial}{\partial x} \delta \psi_x + N_{\theta\theta} \left(\frac{1}{R} \frac{\partial}{\partial \theta} \delta v + \frac{1}{R} \delta w \right) \\ + \frac{1}{R} M_{\theta\theta} \frac{\partial}{\partial \theta} \delta \psi_\theta + Q_{xz} \left(\delta \psi_x + \frac{\partial}{\partial x} \delta w \right) + N_{x\theta} \left(\frac{1}{R} \frac{\partial}{\partial \theta} \delta u + \frac{\partial}{\partial x} \delta v \right) \\ + M_{x\theta} \left(\frac{1}{R} \frac{\partial}{\partial \theta} \delta \psi_x + \frac{\partial}{\partial x} \delta \psi_\theta \right) + Q_{z\theta} \left(\delta \psi_\theta + \frac{1}{R} \frac{\partial}{\partial \theta} \delta w - \frac{1}{R} \delta v \right) \end{array} \right\} R \, dx \, d\theta$$

$$+ \int_0^{2\pi} \int_0^L \int_{-h_p/2}^{h_p/2} \left[\begin{array}{l} -D_x \left\{ \cos(\beta z) \frac{\partial}{\partial x} \delta \phi \right\} \\ -D_\theta \left(\frac{1}{R+z} \right) \left\{ \cos(\beta z) \frac{\partial}{\partial \theta} \delta \phi \right\} \\ +D_z (\beta \sin(\beta z) \phi) \end{array} \right] R \, dx \, dz \, d\theta \tag{24}$$

where the force and momentum resultants are:

$$\{ N_{xx}, N_{\theta\theta}, N_{x\theta} \} = \int_{-h_{ff}/2}^{h_{eff}/2} \{ t_{xx}, t_{\theta\theta}, t_{x\theta} \} \, dz$$

$$\{ M_{xx}, M_{\theta\theta}, M_{x\theta} \} = \int_{-h_{ff}/2}^{h_{ff}/2} \{ t_{xx}, t_{\theta\theta}, t_{x\theta} \} z \, dz \tag{25}$$

$$\{ Q_{xz}, Q_{\theta z} \} = \int_{-h_{ff}/2}^{h_{ff}/2} k_s \{ t_{xz}, t_{\theta z} \} \, dz, \quad k_s = 5/6$$

Governing equations for a cylindrical shell based on the FSDT and nonlocal strain gradient theory are derived by substituting Eqs. (20), (23) and (24) into Eq. (19) and integrating by parts.

$$\delta u : N_{xx,x} + \frac{N_{x\theta,\theta}}{R} + X_{31} \phi_{,x} = \left(I_0 u_{,t^2} + I_1 \psi_{x,t^2} \right) \tag{26}$$

$$\delta v : N_{x\theta,x} + \frac{N_{\theta\theta,\theta}}{R} + \frac{Q_{z\theta}}{R} + \frac{X_{61}}{R} \phi_{,\theta}$$
$$- \frac{k_s X_{24}}{R} \phi_{,\theta} - N_1^P v_{,x^2} = \left(I_0 v_{,t^2} + I_1 \psi_{\theta,t^2} \right) \tag{27}$$

$$\delta w : Q_{xz,x} + \frac{Q_{z\theta,\theta}}{R} - \frac{N_{\theta\theta}}{R} - \frac{k_s X_{24}}{R} \phi_{,\theta^2}$$
$$- k_s X_{15} \phi_{,x^2} - N_1^P w_{,x^2} - \frac{(Y_{xx,\theta x} - Y_{\theta\theta,x\theta})}{2R} = I_0 w_{,t^2} \tag{28}$$

$$\delta \psi_x : M_{xx,x} + \frac{M_{\theta\theta,\theta}}{R} - Q_{xz} + X_{32} \phi_{,x} + k_s X_{12} \phi_{,x} = \left(I_1 u_{,t^2} + I_2 \psi_{x,t^2} \right) \tag{29}$$

$$\delta \psi_\theta : \frac{M_{\theta\theta,\theta}}{R} + M_{x\theta,x} - Q_{z\theta} + \frac{X_{62}}{R} \phi_{,\theta} + k_s X_{13} \phi_{,\theta} = \left(I_1 v_{,t^2} + I_2 \psi_{\theta,t^2} \right) \tag{30}$$

$$\delta \phi : \int_{-h/2}^{h/2} \left\{ D_{x,x} \cos(\beta z) + D_{\theta,\theta} \frac{\cos(\beta z)}{R+z} + D_z \beta \sin(\beta z) \right\} dz = 0 \tag{31}$$

Also, the parameters used in Eq. (31) are expressed as:

$$\int_{-h_p/2}^{h_p/2} D_x \cos(\beta z) = X_{11}\phi_{,x} + X_{12}(\psi_x + w_{,x}),$$

$$\int_{-h_p/2}^{h_p/2} D_\theta \frac{\cos(\beta z)}{R+z} = X_{22}\phi_{,\theta} + X_{13}\left(\psi_\theta + \frac{1}{R}w_{,\theta} - \frac{v}{R}\right),$$

$$\int_{-h_p/2}^{h_p/2} D_z \beta \sin(\beta z) = -X_{33}\phi + X_{31}u_{,x} + X_{32}\psi_{x,x} + X_{61}\left(\frac{1}{R}v_{,\theta} + \frac{w}{R}\right) + X_{62}\left(\frac{\psi_{\theta,\theta}}{R}\right). \tag{32}$$

where

$$X_{11} = \int_{-h/2}^{h/2} \{s_{11e}\}(\cos(\beta z))^2 \mathrm{d}z, \quad X_{22} = \int_{-h/2}^{h/2} \{s_{22e}\}\left(\frac{\cos(\beta z)}{R+z}\right)^2 \mathrm{d}z,$$

$$X_{13} = \int_{-h/2}^{h/2} \frac{\cos(\beta z)}{R+z} e_{24e} \mathrm{d}z, \quad X_{33} = \int_{-h/2}^{h/2} \{s_{33e}\}(\beta \sin(\beta z))^2 \mathrm{d}z, \tag{33}$$

$$\{X_{31}, X_{32}\} = \int_{-h/2}^{h/2} \{1, z\}\beta \sin(\beta z) e_{31e} \mathrm{d}z, \quad \{X_{61}, X_{62}\} = \int_{-h/2}^{h/2} \{1, z\}\beta \sin(\beta z) e_{32e} \mathrm{d}z.$$

In addition, associated boundary conditions are as below:

$$\delta u_0 = 0 \quad \text{or} \quad N_{xx}\mathrm{d}\theta + \frac{N_{x\theta}}{R}\mathrm{d}x = 0$$

$$\delta v_0 = 0 \quad \text{or} \quad N_{x\theta}\mathrm{d}\theta + \frac{N_{\theta\theta}}{R}\mathrm{d}x = 0$$

$$\delta w_0 = 0 \quad \text{or} \quad Q_{xz}\mathrm{d}\theta + \frac{Q_{\theta z}}{R}\mathrm{d}x = 0 \tag{34}$$

$$\delta u_1 = 0 \quad \text{or} \quad M_{xx}\mathrm{d}\theta + \frac{M_{x\theta}}{R}\mathrm{d}x = 0$$

$$\delta v_1 = 0 \quad \text{or} \quad M_{x\theta}\mathrm{d}\theta + \frac{M_{\theta\theta}}{R}\mathrm{d}x = 0$$

3 Solution procedure

Displacement fields for investigation the wave propagation analysis of the structure defined as follow:

$$\begin{Bmatrix} U(x,\theta,z,t) \\ V(x,\theta,z,t) \\ W(x,\theta,z,t) \\ \psi_x(x,\theta,z,t) \\ \psi_\theta(x,\theta,z,t) \end{Bmatrix} = \begin{Bmatrix} u_0 \exp(mx + n\theta - \omega t)i \\ v_0 \exp(mx + n\theta - \omega t)i \\ w_0 \exp(mx + n\theta - \omega t)i \\ \psi_{x_0} \exp(mx + n\theta - \omega t)i \\ \psi_{\theta_0} \exp(mx + n\theta - \omega t)i \end{Bmatrix} \tag{35}$$

where $u_0, v_0, w_0, \psi_{x_0}$ and ψ_{θ_0} are wave amplitude parameters. m and n are wave number along the directions of x and θ, respectively, also ω is called frequency. With replacing Eq. (35) into Eqs. (26–31) achieve to:

$$([K] - \omega^2[M])\{d\} = \{0\} \tag{36}$$

where K and M are the stiffness and mass matrixes, respectively. Also,

$$\{d\} = \begin{Bmatrix} u_0 & v_0 & w_0 & \psi_{x_0} & \psi_{\theta_0} \end{Bmatrix} \tag{37}$$

In addition, the phase velocity of wave dispersion can be calculated by Eq. (30):

$$c = \frac{\omega}{m} \tag{38}$$

In Eq. (38), c and m are called phase velocity and wave number of a laminated nanocomposite cylindrical shell. These parameters are propagation speeds of the particles in a laminated nanocomposite cylindrical shell. With considering $\mu = 0$, the phase velocity of classical continuum theory is computed.

3.1 Parametric study

Results section are presented by two sections, the first section studies the verifications of the results with those available in the literature. The second section presents the influence of GPL distribution pattern, applied voltage and GPL weight function on phase velocity of the GPLRC cylindrical nanoshell coupled with PIAC. The material properties of the GPLRC nanoshell are summarized in Table 1.

Table 1 Material properties of the epoxy and GPL [66]

Material properties	Epoxy	GPL
Young's modulus (GPa)	3	1010
Density (kg m^{-3})	1200	1062.5
Poisson's ratio	0.34	0.186

Table 2 Material properties of piezoelectric layer which is composed of $BiTiO_3$–$CoFeO_4$ [40]

Material constants	$BiTiO_3$–$CoFeO_4$
Elastic (GPa)	$c_{11} = 226,\ c_{12} = 125,\ c_{13} = 124,\ c_{33} = 216,\ c_{44} = 44.2,$ $c_{55} = 44.2,\ c_{66} = 50.5$
Piezoelectric (C m^{-2})	$e_{31} = -2.2,\ e_{33} = 9.3,\ e_{15} = 5.8$
Dielectric (10^{-9} C V m^{-1})	$s_{11} = 5.64,\ s_{22} = 5.64,\ s_{33} = 6.35$
Piezomagnetic (N A m^{-1})	$q_{15} = 275,\ q_{31} = 290.1,\ q_{33} = 349.9$
Magnetoelectric (10^{-12} N V C^{-1})	$d_{11} = 5.367,\ d_{33} = 2737.5$
Magnetic (10^{-6} Ns^2 C^{-2})	$r_{11} = -297,\ r_{33} = 83.5$
Thermal moduli (10^5 N km^{-2})	$\beta_1 = 4.74,\ \beta_3 = 4.53$
Pyroelectric (10^{-6} C N^{-1})	$P_3 = 25$
Pyromagnetic (10^{-6} N A m K^{-1})	$\lambda_3 = 5.19$
Mass density (10^3 kg m^{-3})	$\rho = 5.55$

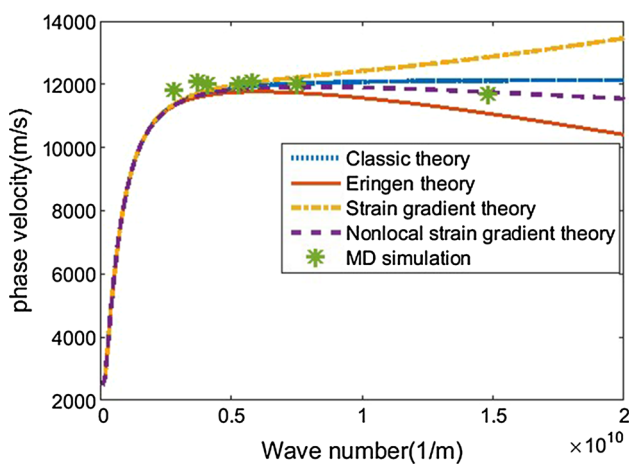**Fig. 7** The comparison of phase velocity obtained by current study and MD simulation [50] for different wave numbers and continuum theories
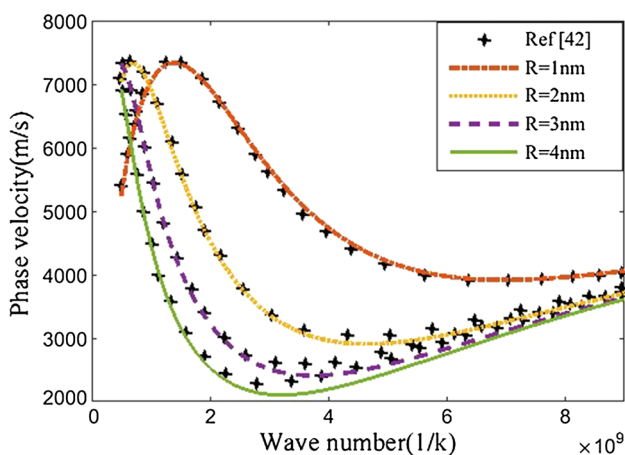

Fig. 8 Comparison of phase velocity of isotropic homogeneous nanoshells, with different parameters

In addition, the material properties of the piezoelectric layer are given in Table 2.

As discussed in introduction section, a reliable approach to assess the validity of results estimated by various size-dependent theories is to compare them with those of molecular dynamics simulation. In this regard, Fig. 7 displays the variation of phase velocity versus phase number, estimated by different continuum theories of the present study and MD simulation of Ref. [48] for (15, 15) single-walled carbon nanotube. According to this figure from $k = 0$ to about $s = 0.5$ (1/m), with increasing the wave number all theories show a similar increase in phase velocity. Afterward, classic theory estimates the phase velocity remains constant, while Eringen and strain gradient theories estimate a steady decrease and increase in phase velocity, respectively. The best consistency with MD simulation is resulted by choosing the appropriate size-dependent parameters ($\mu = 0.55$ nm, $l = 0.35$ nm) of nonlocal strain gradient theory which shows a gentle decrease in phase velocity. Another validation is presented in Fig. 8 indicating the effect of radius on phase velocity for a SWCNT with $R/h = 12$, $\mu = 0.55$ nm, $l = 0.35$ nm, $E = 0.83$ GPa; $= 2270$; $= 0.317$; $n = 1$. As illustrated, results of the present study are of accurate agreement with those of Ref [67] especially in smaller radiuses of SWCNT.

As a parametric study in this section of the current article, effects of different PIAC thickness, pattern of GNP, mode numbers and applied voltage on the phase velocity of the nanostructure are studied in Table 3. It is observed that all patterns of GNP reinforcement in comparison with pure epoxy show the higher values of phase velocity in a cylindrical nanoshell. This is because, by adding GNP reinforcement in the structure, the stability increases. Also, it can be found from this result that, effect of applied voltage on the phase velocity of the nanostructures is inverse. It can be seen from the table that for all values of PIAC thickness and mode number the phase velocities of the nanostructures with GPL

Table 3 The effect of different PIAC thickness, pattern of GNP and mode numbers on phase velocity (km/s) of GNPRC nanoshell with $s = 1(1/nm)$, $g_{GPL} = 1\%$, $R = 1$ nm, $h = R/10$

|	$n = 1$		$n = 2$		$n = 3$	
	$h_p = h/20$	$h_p = h/10$	$h_p = h/20$	$h_p = h/10$	$h_p = h/20$	$h_p = h/10$
Pure epoxy						
Φ (mVolt)						
0	0.950952	1.135213	0.571641	0.671976	0.750838	0.852311
1	0.897843	1.098203	0.477231	0.607062	0.682519	0.802453
2	0.841338	1.059881	0.359352	0.534309	0.606549	0.749282
3	0.780703	1.020101	0.174627	0.449928	0.519583	0.692037
Pattern 1						
Φ (mVolt)						
0	1.353548	1.438770	0.846692	0.883556	1.207535	1.217339
1	1.316756	1.409735	0.782695	0.835218	1.166244	1.182940
2	1.278890	1.380079	0.720790	0.783900	1.123434	1.147509
3	1.239851	1.349763	0.648726	0.728973	1.078926	1.110948
Pattern 2						
Φ (mVolt)						
0	1.352978	1.438318	0.825098	0.866104	1.120738	1.144654
1	1.316169	1.409273	0.762958	0.816729	1.076119	1.107998
2	1.278284	1.379607	0.695278	0.764165	1.029565	1.070087
3	1.239225	1.349279	0.620248	0.707703	0.980804	1.030781
Pattern 3						
Φ (mVolt)						
0	1.354507	1.439530	0.867739	0.900698	1.287439	1.285275
1	1.317744	1.410512	0.808897	0.853336	1.248794	1.252744
2	1.279909	1.380875	0.745417	0.803181	1.208915	1.219345
3	1.240904	1.350578	0.675993	0.749674	1.167672	1.185005
Pattern 4						
Φ (mVolt)						
0	1.354502	1.439649	0.835099	0.875785	1.168384	1.191728
1	1.317731	1.410579	0.773634	0.826913	1.125595	1.156530
2	1.279835	1.380888	0.706837	0.774960	1.081113	1.120225
3	1.240731	1.350535	0.633021	0.719259	1.034719	1.082703
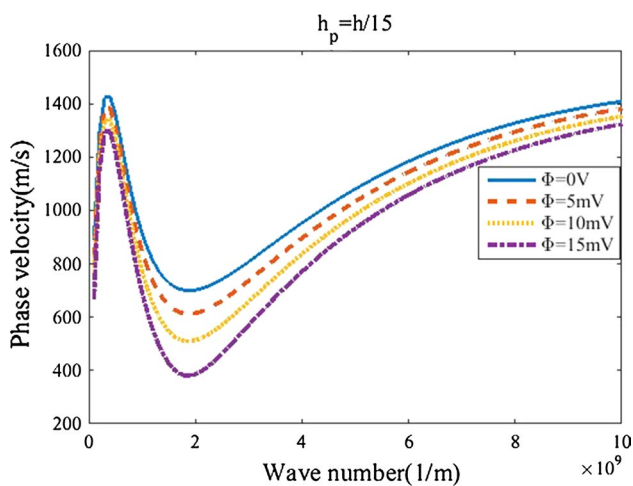
Fig. 9 Effect of external applied voltage and wave number on the phase velocity of the GNPRC nanoshell coupled with PIAC with $h_p = h/15$
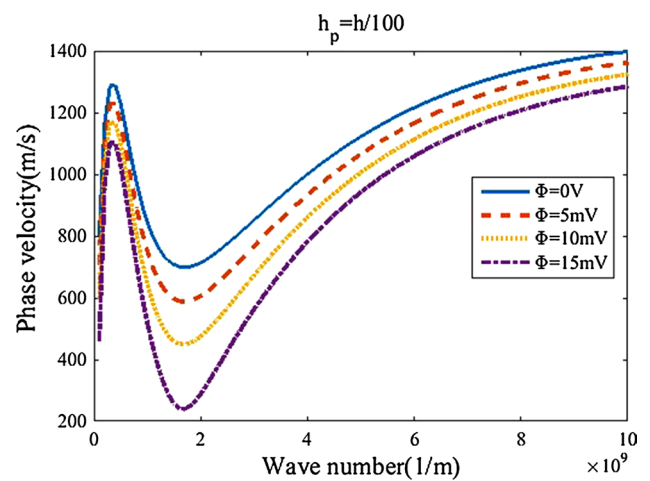

Fig. 10 Effect of external applied voltage and wave number on the phase velocity of the GNPRC nanoshell coupled with PIAC with $h_p = h/100$

distribution pattern 3 are higher than in comparison with other patterns. This result shows an increase in the stability of nanostructures with GPL distribution pattern 3. In other words, O-GPLRC gives larger value of the phase velocity than other patterns. The reason for this issue is in the mathematical function which is presented in the previous section. Besides, it is clearly seen from Table 3 that PIAC thickness and pattern of GNP have direct effects on the phase velocity. Also, by increasing the mode number from first to second, the phase velocity increases but changing from second to third, this behavior is inverse.

Figures 9 and 10 present the effects of PIAC thickness and applied voltage on phase velocity of a GNPRC nanoshell covered by PIAC with $R = 4$ nm, $h = R/10$, $= 0.055$ nm, $l = 0.03$ nm and $g_{GPL} = 1\%$. According to Figs. 9 and 10, from one of these graphs (for a specific value of PIAC thickness and applied voltage), it can be found that first by increasing wave number the phase velocity increases. After a maximum value of the phase velocity, by increasing the wave number, the phase velocity decreases until the phase velocity reaches a minimum value.

After the minimum value, phase velocity is improved with increasing the wave number. Figures 8 and 9 demonstrate that, by decreasing the PIAC thickness, the minimum and maximum values of the phase velocity shift to left. For a better comprehensive, by decreasing the PIAC thickness, extremum values of phase velocity are seen in the lower values of the wave number. As an important result, by decreasing the PIAC thickness, the phase velocity decreases in the all range of the wave number. In addition, by increasing the applied voltage, the phase velocity decreases in the all range of the wave number. As a comparison report, the PIAC
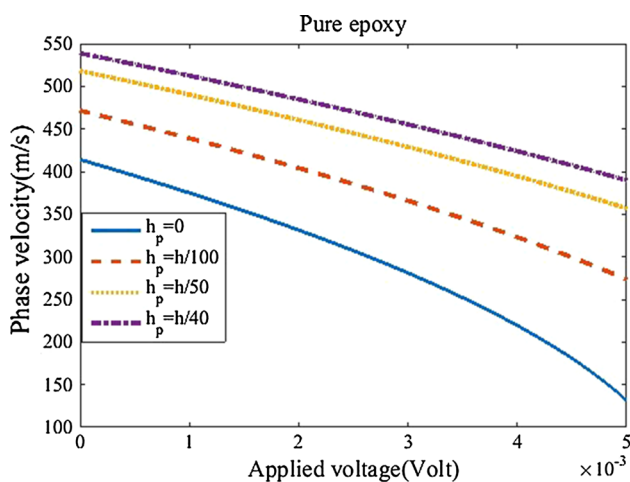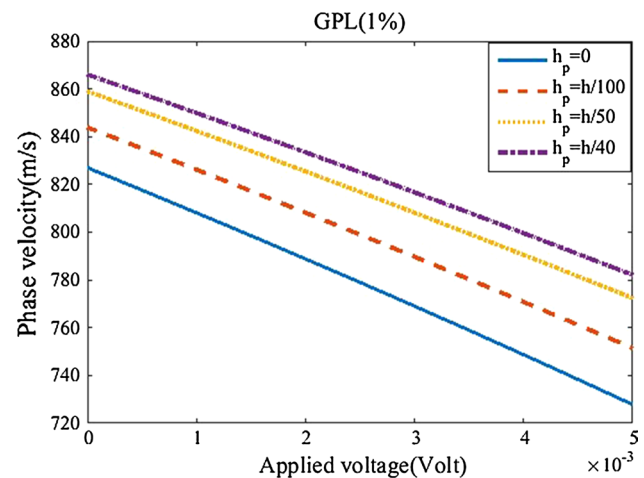

Fig. 12 Effect of PIAC thickness and external applied voltage on the phase velocity of the GPLRC cylindrical nanoshell coupled with PIAC

thickness and applied voltage have direct and inverse effects on the phase velocity of the nanostructure, respectively. Furthermore, as a new report of literature, comparison of the effects of PIAC thickness and applied voltage on the phase velocity can be found from these figures which show that by decreasing the effect of PIAC thickness the effect of applied voltage on the phase velocity become more significant. In another word, these figures show that, by increasing the PIAC thickness, the graphs of Fig. 9 are closely than the graphs of Fig. 10. As a useful suggestion of this research is that for designing of a nanostructure coupled with PIAC should be attention to the PIAC thickness and applied voltage, simultaneously. It is worth to mention that increasing the PIAC thickness and applied voltage has negative and positive effects on the stability of the nanostructure, respectively.

Figures 11 and 12 present the phase velocity of GNPRC nanoshell (pattern 2, 1% GNP, $R = 4$ nm and $h = R/10$) covered by PIAC and pure epoxy ($R = 4$ nm and $h = R/10$) for different values of PIAC thickness and applied voltage. These figures explain that, for high value of applied voltage, by increasing this parameter the phase velocity of those nanostructures decreases with an extremely rate. As described in the previous section, Figs. 9 and 10 represent that, by increasing the PIAC thickness, the phase velocity of both nanoshells increases in the all ranges of the applied voltage. Besides, by comparing these figures, the phase velocity of the GNPRC nanoshells is more than pure epoxy nanoshells. As a significant suggestion from this result, it can be found that, by adding GNP in the pure epoxy matrix the dynamic behaviors (phase velocity) of the structure improves. It is worth to mention that, for pure epoxy nanoshells coupled with PIAC, changes of phase velocity
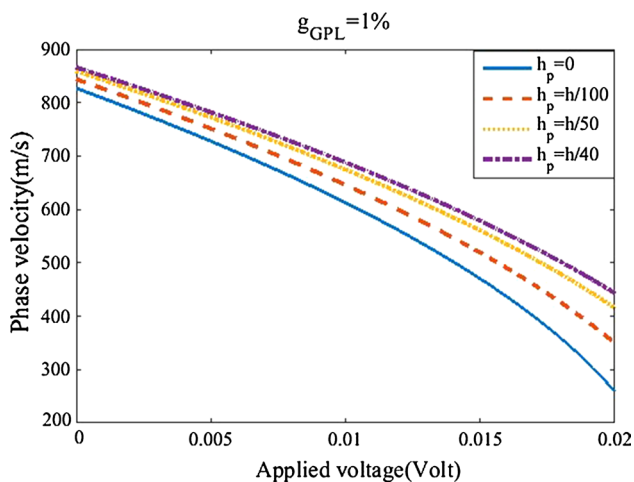

Fig. 11 Effect of PIAC thickness and external applied voltage on the phase velocity of the pure epoxy cylindrical nanoshell coupled with PIAC

Fig. 13 Effect of PIAC thickness and external applied voltage on the phase velocity of the GPLRC cylindrical nanoshell with $g_{GPL} = 1\%$
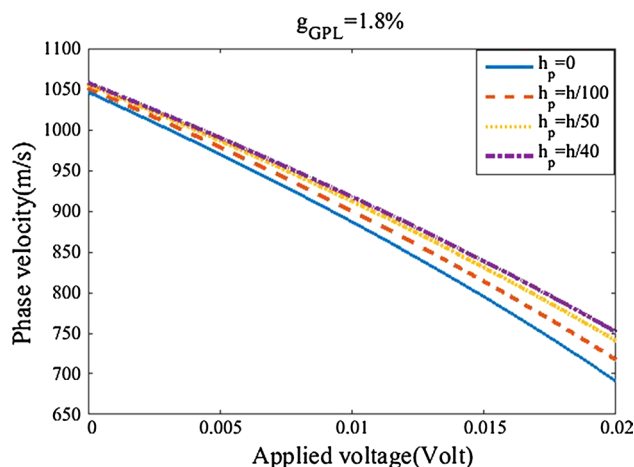

Fig. 15 Effect of PIAC thickness and external applied voltage on the phase velocity of the GPLRC cylindrical nanoshell with $g_{GPL} = 1.8\%$
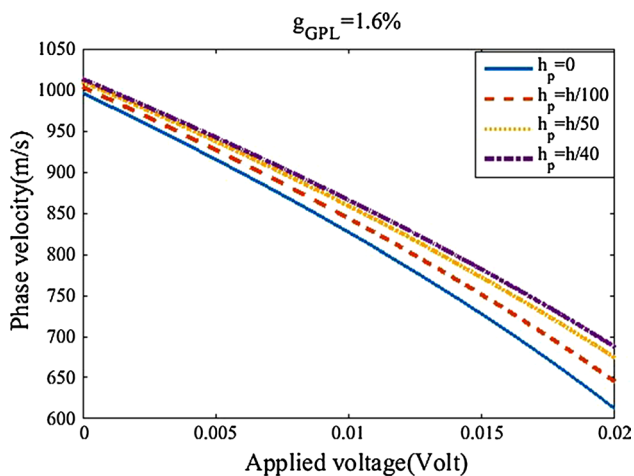

Fig. 14 Effect of PIAC thickness and external applied voltage on the phase velocity of the GPLRC cylindrical nanoshell with $g_{GPL} = 1.6\%$
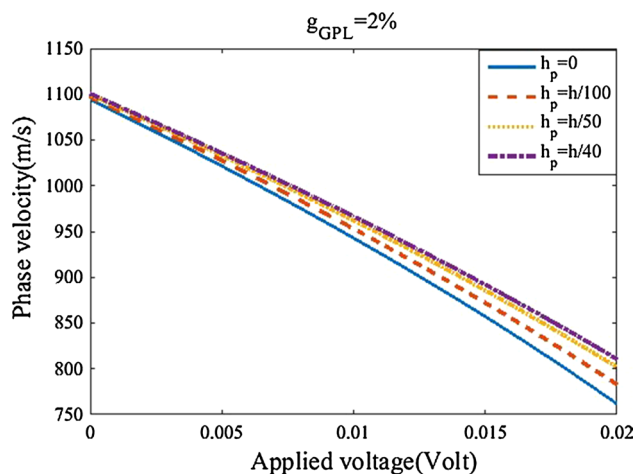

Fig. 16 Effect of PIAC thickness and external applied voltage on the phase velocity of t he GPLRC cylindrical nanoshell with $g_{GPL} = 2\%$

with increasing applied voltage is nonlinear, especially for high values of PIAC thickness, while this behavior for GNPRC nanoshells actuated with piezoelectric is linear in every value of PIAC thickness. This result is a reaffirm that, GPL in the epoxy matrix can prevent from nonlinear changes and transform the nonlinear to linear changes.

Figures 13, 14, 15 and 16 present the effects of different GPL percentages, PIAC thickness and applied voltage on phase velocity of a GNPRC nanoshell covered by PIAC with $R = 4$ nm, $h = R/10$, $\mu = 0.055$ nm, $l = 0.03$ nm and pattern 2. All of these figures show that, with enhancement the nanostructures (GNPRC nanoshell actuated by piezoelectric layer) by increasing the GPL%, the phase velocity of the nanostructures can be improved for all ranges of applied voltage and all values of the PIAC thickness. This result

demonstrates another advantage of GNP. For low value of the GNP% and different PIAC thickness, changing of phase velocity with increasing applied voltage is in nonlinear form but by increasing the GNP% this nonlinear behavior can be similar to the linear. An amazing result is that, in the lower values of applied voltage in comparison with higher ones, the effect of PIAC thickness decreases. Another important result is that, by increasing GPL%, the effects of PIAC thickness on the phase velocity decreases.

4 Conclusion

This article studies the wave propagation electrical characteristics of a size-dependent GNPRC cylindrical nanoshell coupled with PIAC using NSGT. The governing equations of nanostructure have been evolved using Hamilton's principle and solved with assistance of the analytical method. For the first time in the current study, wave propagation-electrically characteristics of a GNPRC cylindrical shell coupled with PIAC based on an exact size-dependent continuum theory is examined. Finally, influence of wave number, critical voltage, PIAC thickness and different GNP distribution patterns on phase velocity are investigated using mentioned continuum mechanics theory. In this work, the following main results can be achieved:

1. The results show that, by decreasing the PIAC thickness, extremum values of the phase velocity occur in the lower values of the wave number.
2. It is observed that, by increasing GPL%, the effects of PIAC thickness on the phase velocity decrease.
3. The PIAC thickness and applied voltage have direct and inverse effects on the phase velocity of the nanostructure, respectively.
4. The results demonstrate that, by adding GNP in the pure epoxy matrix, the phase velocity of the nanostructure improves.
5. Another important result is that, by increasing GPL%, the effects of PIAC thickness on the phase velocity decrease.

References

1. Shi G et al (2018) Graphene platelets and their polymer composites: fabrication, structure, properties, and applications. Adv Funct Mater 28(19):1706705
2. Sun J, Zhao J (2018) Multi-layer graphene reinforced nano-laminated WC-Co composites. Mater Sci Eng A 723:1–7
3. Nieto A, Lahiri D, Agarwal A (2013) Graphene NanoPlatelets reinforced tantalum carbide consolidated by spark plasma sintering. Mater Sci Eng A 582:338–346
4. Rafiee MA et al (2009) Enhanced mechanical properties of nanocomposites at low graphene content. ACS Nano 3(12):3884–3890
5. Shahsavari D, Janghorban M (2017) Bending and shearing responses for dynamic analysis of single-layer graphene sheets under moving load. J Braz Soc Mech Sci Eng 39(10):3849–3861
6. Shokrani MH et al (2016) Buckling analysis of double-orthotropic nanoplates embedded in elastic media based on non-local two-variable refined plate theory using the GDQ method. J Braz Soc Mech Sci Eng 38(8):2589–2606
7. Shahrjerdi A, Yavari S (2018) Free vibration analysis of functionally graded graphene-reinforced nanocomposite beams with temperature-dependent properties. J Braz Soc Mech Sci Eng 40(1):25
8. Kumar J, Mondal S (2018) Microstructure and properties of graphite-reinforced copper matrix composites. J Braz Soc Mech Sci Eng 40(4):196
9. Anas M et al (2018) Structural health monitoring of GFRP laminates using graphene-based smart strain gauges. J Braz Soc Mech Sci Eng 40(8):397
10. Habibi M et al (2018) Forming limit diagrams by including the M–K model in finite element simulation considering the effect of bending. Proc Inst Mech Eng Part L J Mater Des Appl 232(8):625–636
11. Habibi M et al (2018) Experimental investigation of mechanical properties, formability and forming limit diagrams for tailor-welded blanks produced by friction stir welding. J Manuf Process 31:310–323
12. Habibi M et al (2016) Enhancing the mechanical properties and formability of low carbon steel with dual-phase microstructures. J Mater Eng Perform 25(2):382–389
13. Habibi M et al (2017) Determination of forming limit diagram using two modified finite element models. Mech Eng 48(4):141–144
14. Ghazanfari A et al (2016) Investigation on the effective range of the through thickness shear stress on forming limit diagram using a modified Marciniak–Kuczynski model. Modares Mech Eng 16(1):137–143
15. Dong Y et al (2018) Nonlinear free vibration of graded graphene reinforced cylindrical shells: effects of spinning motion and axial load. J Sound Vib 437:79–96
16. Dong Y et al (2018) Buckling of spinning functionally graded graphene reinforced porous nanocomposite cylindrical shells: an analytical study. Aerosp Sci Technol 82:466–478
17. Dong Y et al (2018) Vibration characteristics of functionally graded graphene reinforced porous nanocomposite cylindrical shells with spinning motion. Compos B Eng 145:1–13
18. Yang J, Wu H, Kitipornchai S (2017) Buckling and postbuckling of functionally graded multilayer graphene platelet-reinforced composite beams. Compos Struct 161:111–118
19. Feng C, Kitipornchai S, Yang J (2017) Nonlinear bending of polymer nanocomposite beams reinforced with non-uniformly distributed graphene platelets (GPLs). Compos B Eng 110:132–140
20. Barooti MM, Safarpour H, Ghadiri M (2017) Critical speed and free vibration analysis of spinning 3D single-walled carbon nanotubes resting on elastic foundations. Eur Phys J Plus 132(1):6
21. SafarPour H, Ghadiri M (2017) Critical rotational speed, critical velocity of fluid flow and free vibration analysis of a spinning SWCNT conveying viscous fluid. Microfluid Nanofluid 21(2):22
22. Ghashami G et al (2016) An exact solution for size-dependent frequencies of micro-beam resonators by considering the thermoelastic coupling terms. J Braz Soc Mech Sci Eng 38(7):1947–1957
23. Karimipour I et al (2016) Using couple stress theory for modeling the size-dependent instability of double-sided beam-type nanoactuators in the presence of Casimir force. J Braz Soc Mech Sci Eng 38(6):1779–1795
24. Zeighampour H, Shojaeian M (2017) Size-dependent vibration of sandwich cylindrical nanoshells with functionally graded material based on the couple stress theory. J Braz Soc Mech Sci Eng 39(7):2789–2800
25. Mehralian F, Beni YT (2018) Vibration analysis of size-dependent bimorph functionally graded piezoelectric cylindrical shell based on nonlocal strain gradient theory. J Braz Soc Mech Sci Eng 40(1):27
26. Safarpour H, Hajilak ZE, Habibi M (2018) A size-dependent exact theory for thermal buckling, free and forced vibration analysis of temperature dependent FG multilayer GPLRC composite nanostructures restring on elastic foundation. Int J Mech Mater Des. https://doi.org/10.1007/s10999-018-9431-8

27. Ghadiri M, Shafiei N, Safarpour H (2017) Influence of surface effects on vibration behavior of a rotary functionally graded nanobeam based on Eringen's nonlocal elasticity. Microsyst Technol 23(4):1045–1065

28. Ghadiri M, SafarPour H (2017) Free vibration analysis of size-dependent functionally graded porous cylindrical microshells in thermal environment. J Therm Stress 40(1):55–71

29. SafarPour H et al (2017) Influence of various temperature distributions on critical speed and vibrational characteristics of rotating cylindrical microshells with modified lengthscale parameter. Eur Phys J Plus 132(6):281

30. Safarpour H, Mohammadi K, Ghadiri M (2017) Temperature-dependent vibration analysis of a FG viscoelastic cylindrical microshell under various thermal distribution via modified length scale parameter: a numerical solution. J Mech Behav Mater 26(1–2):9–24

31. Safarpour H, Ghanizadeh SA, Habibi M (2018) Wave propagation characteristics of a cylindrical laminated composite nanoshell in thermal environment based on the nonlocal strain gradient theory. Eur Phys J Plus 133(12):532

32. Ebrahimi F, Habibi M, Safarpour H (2018) On modeling of wave propagation in a thermally affected GNP-reinforced imperfect nanocomposite shell. Eng Comput. https://doi.org/10.1007/s00366-018-0669-4

33. Khorshidi MA, Shariati M (2016) Free vibration analysis of sigmoid functionally graded nanobeams based on a modified couple stress theory with general shear deformation theory. J Braz Soc Mech Sci Eng 38(8):2607–2619

34. Wang Y-G et al (2017) Large deflection analysis of functionally graded circular microplates with modified couple stress effect. J Braz Soc Mech Sci Eng 39(3):981–991

35. Some S, Guha SK (2018) Effect of slip and percolation of polar additives of coupled-stress lubricant on the steady-state characteristics of double-layered porous journal bearings. J Braz Soc Mech Sci Eng 40(2):68

36. Moshir SK, Eipakchi H (2016) An analytical procedure for transient response determination of annular FSDT and CPT nanoplates via nonlocal elasticity theory. J Braz Soc Mech Sci Eng 38(8):2277–2288

37. Pourjabari A et al. (2019) Effect of porosity on free and forced vibration characteristics of the GPL reinforcement composite nanostructures. Comput Math Appl. https://doi.org/10.1016/j.camwa.2018.12.041

38. Ghadiri M, Safarpour H (2016) Free vibration analysis of embedded magneto-electro-thermo-elastic cylindrical nanoshell based on the modified couple stress theory. Appl Phys A 122(9):833

39. Shojaeefard M et al (2018) Free vibration of an ultra-fast-rotating-induced cylindrical nano-shell resting on a Winkler foundation under thermo-electro-magneto-elastic condition. Appl Math Model 61:255–279

40. SafarPour H, Ghanbari B, Ghadiri M (2018) Buckling and free vibration analysis of high speed rotating carbon nanotube reinforced cylindrical piezoelectric shell. Appl Math Model. https://doi.org/10.1016/j.apm.2018.08.028

41. Safarpour H et al (2018) Effect of porosity on flexural vibration of CNT-reinforced cylindrical shells in thermal environment using GDQM. Int J Struct Stab Dyn 18:1850123

42. Gul U, Aydogdu M (2017) Wave propagation in double walled carbon nanotubes by using doublet mechanics theory. Physica E 93:345–357

43. Arda M, Aydogdu M (2016) Torsional wave propagation in multiwalled carbon nanotubes using nonlocal elasticity. Appl Phys A 122(3):219

44. Islam Z, Jia P, Lim C (2014) Torsional wave propagation and vibration of circular nanostructures based on nonlocal elasticity theory. Int J Appl Mech 6(02):1450011

45. Aydogdu M (2014) Longitudinal wave propagation in multiwalled carbon nanotubes. Compos Struct 107:578–584

46. Lim C, Zhang G, Reddy J (2015) A higher-order nonlocal elasticity and strain gradient theory and its applications in wave propagation. J Mech Phys Solids 78:298–313

47. Lu L, Guo X, Zhao J (2017) Size-dependent vibration analysis of nanobeams based on the nonlocal strain gradient theory. Int J Eng Sci 116:12–24

48. Ebrahimi F, Barati MR (2016) Vibration analysis of nonlocal beams made of functionally graded material in thermal environment. Eur Phys J Plus 131(8):279

49. Mohammadi K et al (2018) Cylindrical functionally graded shell model based on the first order shear deformation nonlocal strain gradient elasticity theory. Microsyst Technol 24(2):1133–1146

50. Zeighampour H, Beni YT, Karimipour I (2017) Wave propagation in double-walled carbon nanotube conveying fluid considering slip boundary condition and shell model based on nonlocal strain gradient theory. Microfluid Nanofluid 21(5):85

51. Zeighampour H, Beni YT, Karimipour I (2017) Material length scale and nonlocal effects on the wave propagation of composite laminated cylindrical micro/nanoshells. Eur Phys J Plus 132(12):503

52. Zeighampour H, Beni YT, Dehkordi MB (2018) Wave propagation in viscoelastic thin cylindrical nanoshell resting on a visco-Pasternak foundation based on nonlocal strain gradient theory. Thin Walled Struct 122:378–386

53. Gaur AM, Rana DS (2014) Shear wave propagation in piezoelectric-piezoelectric composite layered structure. Lat Am J Solids Struct 11(13):2483–2496

54. Ghorbanpour Arani A et al (2017) Analytical modeling of wave propagation in viscoelastic functionally graded carbon nanotubes reinforced piezoelectric microplate under electro-magnetic field. Proc Inst Mech Eng Part N J Nanomater Nanoeng Nanosyst 231(1):17–33

55. Zhou Y (2015) The surface effect on axisymmetric wave propagation in piezoelectric cylindrical shells. Adv Mech Eng 7(2):1687814014568503

56. Bisheh HK, Wu N (2019) Wave propagation in smart laminated composite cylindrical shells reinforced with carbon nanotubes in hygrothermal environments. Compos B Eng 162:219–241

57. Bisheh HK, Wu N (2019) Wave propagation in piezoelectric cylindrical composite shells reinforced with angled and randomly oriented carbon nanotubes. Compos B Eng 160:10–30

58. Bisheh HK, Wu N (2018) Analysis of wave propagation characteristics in piezoelectric cylindrical composite shells reinforced with carbon nanotubes. Int J Mech Sci 145:200–220

59. Bisheh HK, Wu N (2018) Wave propagation characteristics in a piezoelectric coupled laminated composite cylindrical shell by considering transverse shear effects and rotary inertia. Compos Struct 191:123–144

60. Guo X et al (2018) Effects of functionally graded interlayers on dispersion relations of shear horizontal waves in layered piezoelectric/piezomagnetic cylinders. Appl Math Model 55:569–582

61. Yahia SA et al (2015) Wave propagation in functionally graded plates with porosities using various higher-order shear deformation plate theories. Struct Eng Mech 53(6):1143–1165

62. Mahinzare M et al (2017) Size-dependent effects on critical flow velocity of a SWCNT conveying viscous fluid based on nonlocal strain gradient cylindrical shell model. Microfluid Nanofluid 21(7):123

63. Wang Y et al (2018) Torsional buckling of graphene platelets (GPLs) reinforced functionally graded cylindrical shell with cut-out. Compos Struct 197:72–79

64. SafarPour H, Ghanbari B, Ghadiri M (2019) Buckling and free vibration analysis of high speed rotating carbon nanotube reinforced cylindrical piezoelectric shell. Appl Math Model 65:428–442

65. Li X et al (2017) Bending, buckling and vibration of axially functionally graded beams based on nonlocal strain gradient theory. Compos Struct 165:250–265

66. Wu H, Kitipornchai S, Yang J (2017) Thermal buckling and post-buckling of functionally graded graphene nanocomposite plates. Mater Des 132:430–441

67. Li L, Li X, Hu Y (2016) Free vibration analysis of nonlocal strain gradient beams made of functionally graded material. Int J Eng Sci 102:77–92